



HAL
open science

Simulation of fluid driven crack propagation along metal/elastomer interface

P.-Y. Corbel, J Jumel

► **To cite this version:**

P.-Y. Corbel, J Jumel. Simulation of fluid driven crack propagation along metal/elastomer interface: Application to the numerical analysis of the rubber cord adhesion inflation test. *Mechanics of Materials*, 2023, 185, pp.104774. 10.1016/j.mechmat.2023.104774 . hal-04193344

HAL Id: hal-04193344

<https://ensta-bretagne.hal.science/hal-04193344>

Submitted on 5 Sep 2023

HAL is a multi-disciplinary open access archive for the deposit and dissemination of scientific research documents, whether they are published or not. The documents may come from teaching and research institutions in France or abroad, or from public or private research centers.

L'archive ouverte pluridisciplinaire **HAL**, est destinée au dépôt et à la diffusion de documents scientifiques de niveau recherche, publiés ou non, émanant des établissements d'enseignement et de recherche français ou étrangers, des laboratoires publics ou privés.

24 **1. Introduction**

25 Elastomer are used for manufacturing a large variety of parts such as antivibration
26 components, gasket, transmission belt, tires or pipes. To obtain the desired mechanical
27 performances composite systems are often used by incorporating particles, cords, cable, mesh
28 or fabric into an elastomer matrix. However, as for all composite materials the adhesion strength
29 between matrix and reinforcement is a key parameter controlling the overall initial and long
30 terms performances of the component. Specialized techniques are then developed to modify the
31 chemistry and morphology of the surface of the reinforcement so as to achieve strong and
32 durable bonding with the elastomer matrix [1] [2]. Due to more restrictive regulation regarding
33 processes and products toxicity, substantial efforts are undertaken to develop environmentally
34 friendly processes [3]. The mechanical performances of these new reinforcement / elastomer
35 interfaces should be assessed which requires the use of specialized testing protocols.

36 Very few experimental techniques are available to characterize the adhesion between an
37 elastomer matrix and a single reinforcement cords or cable [4] [5] [6] [7] [8]. They are mainly
38 adapted from classical pull out tests and some of them are now standardized (ISO 4647, ISO
39 5603, ASTM D1871-04...). Recently, the rubber cord adhesion inflation test (RCAIT) has been
40 proposed as an alternative technique for refined mechanical characterization of rubber to
41 reinforcement wires bonding [9] [10]. The specimen consists in a unique cord reinforcement
42 embedded along the central axis of a cylindrical rubber envelope and initially partially
43 debonded on one end. A pressurized fluid is slowly introduced in between the rubber envelope
44 and the cord until a critical pressure is reached and a stable and progressive decohesion is
45 observed along the specimen length. To prevent from rubber envelope failure, the specimen is
46 placed in a lubricated confinement tube so as to limits the tube circumferential expansion.
47 Contrary to alternative test procedures, the specimen and test conditions are designed so that a
48 steady state crack propagation regime can be observed when constant pressure of the injected

49 fluid is measured. Then, this test protocol can be viewed as an axisymmetric confined blister
50 test as proposed by [11] [12]. The analysis of such test relies mainly on a global energy balance
51 analysis from which the critical strain energy release rate (SERR) which drives the extension
52 of the decohesion is determined. Basically, the work needed to inject the pressurized fluid is
53 partially stored in the rubber deformation and fluid compression potential energy, the rest being
54 dissipated in the damage processes leading to crack propagation. Other possible dissipation
55 mechanisms can be involved such as rubber envelop damage or viscous dissipation so as fluid
56 viscosity. For this analysis to be valid, crack propagation regime should be stationary. Also, all
57 possible unwanted dissipations mechanisms should be minimized and/or evaluated. At last,
58 some of the quantities needed for the energy balance analysis are determined indirectly from
59 measurable quantities so that possible calibration errors should be evaluated.

60 Due to the axisymmetric nature of the specimen, the fracture process zone surrounding the
61 crack tip region is not visible so that experimental assessment of the RCAIT analysis hypothesis
62 is limited. Then, a finite elements simulation is proposed here to simulate both the crack
63 nucleation and propagation steps and considering the hyperelastic nature of the rubber and
64 complex loading conditions. Indeed, a stationary pressure is recorded during the steady state
65 crack propagation regime. Then, it is necessary to reproduce the fluid driven crack propagation
66 process to ensure the calculations will remain stable. For this reason, fluid cavity elements are
67 used together with cohesive elements to achieve progressive interface decohesion but also to
68 control the fluid injection rate in the numerical simulation. This solution was found relevant to
69 simulate the overall macroscopic response of the specimen during the test and the rubber
70 envelope deformation during the crack propagation process. Alternative specialized
71 implementations have been proposed in other context such as hydraulic fracture simulation,
72 crack propagation in porous media or elastomer using XFEM [13], [14] or phase field [15]
73 implementation. However, no contribution was found where volumetric fluid driven crack

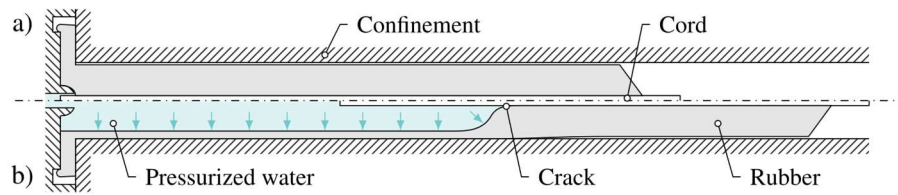
74 propagation along a specific interface and involving hyperelastic material was found. The
75 proposed procedure uses only standard routines implemented in the commercial finite element
76 simulation programme, Abaqus© and could be easily replicated to analyse similar situations.

77 In the following, after a short presentation of the RCAIT principle and analysis, the finite
78 element implementation of the test simulation is described. The results from the model are
79 compared with the ones obtained experimentally and presented in a previous contribution [9].
80 Finally, the self-similar nature of the crack propagation regime is discussed by analysing in
81 details the finite element simulation and by comparing them with the one obtained with the
82 Thich Tube Rubber Inflation Model (TTRIM) [16].

83

84 2. Rubber Cord Adhesion Inflation Test principle

85



86

87 **Figure 1** Rubber cord inflation test in a) initial configuration and b) pre-crack length inflation regime.

88 The rubber cords adhesion inflation test (RCAIT) studied here is depicted in Figure 1.

89 To evaluate the crack nucleation and propagation condition along a metal cord and a rubber

90 matrix, a pressurized fluid is slowly introduced in between the two components. The specimens

91 are obtained by moulding a 9.4mm diameter rubber cylinder around a 1.3mm diameter steel

92 wire coated with brass. During the vulcanization process the rubber creates cohesive bonds with

93 the coating which leads to strong bonding. A release film or anti-adherent coating is placed on

94 one specimen end along a distance $a_0 = 50\text{mm}$ producing an initial decohesion to ease the fluid

95 injection and evaluation of rubber mechanical properties. The specimen geometry also includes

96 a flange on the precrack side which is clamped tightly to a fluid injection fixture connected to

97 a hydraulic circuit. Finally, a glass confinement tube having 10mm inner diameter is placed

98 around the specimen so as to prevent from rubber envelope failure and force the crack

99 propagation along the cord. The tube is lubricated to prevent any adhesion between rubber and

100 glass or at least limit possible friction effect.

101 The test is driven under constant fluid volume injection rate. During the test, the fluid

102 pressure first increases while the precrack part of the specimen envelope inflates. Two regimes

103 are observed here. First the free inflation regime, prior the outer surface of the specimen touches

104 the confinement tube. Then the confined inflation regime, when the specimen is constrained

105 radially and the envelope expands mainly axially. After a critical pressure is reached, the crack

106 propagates a stable manner and the fluid pressure remains almost constant. Tap water is
107 generally used for the experiments.

108 During the test, several quantities can be measured. Fluid pressure, P , is recorded with
109 a pressure sensor placed along the hydraulic circuit. The fluid is injected by using a high-
110 pressure stainless-steel syringe whose piston is attached to a tensile testing machine to control
111 the volume injection rate. The injected volume, ΔV , is determined from the crosshead
112 displacement measurement after a proper calibration of the system is performed to evaluate
113 possible effect of fluid compressibility and hydraulic circuit compliance. Finally, markers
114 and/or patterns are drawn on the specimen and observed during the experiment with a camera
115 in order to monitor the longitudinal elongation, λ_z , at the surface of the specimen.

116 Assuming the initial decohesion is large and contribution of clamping and crack tip
117 regions on the overall deformation is negligible, the measured $P(\Delta V)$ evolutions can be used to
118 evaluate the rubber mechanical behaviour with the help of the thick tube rubber inflation model
119 (TTRIM). Once a critical pressure P_C value is reached a decohesion occurs at/or near the rubber
120 / cord interface. The decohesion then propagates a stable manner longitudinally while the fluid
121 is slowly injected at a constant pressure value. A simple energy balance analysis is then used to
122 evaluate, G_C , which controls the propagation of the decohesion:

123

$$P_C \delta V = 2\pi r_c \cdot G_C \delta a + w_e \delta a \quad (1)$$

124

125 In equation (1), the term $P_C \delta V$ corresponds to the energy transferred to the system when
126 injecting the pressurized fluid and propagating the crack along a distance δa . This energy is
127 converted mainly into potential energy $w_e \delta a$ due to rubber envelope reversible expansion and
128 fluid incompressibility. w_e corresponds to the stored elastic energy per unit length. Finally, a
129 substantial ratio, $2\pi r_c \cdot G_C \delta a$, is dissipated during the fracture process and other dissipative

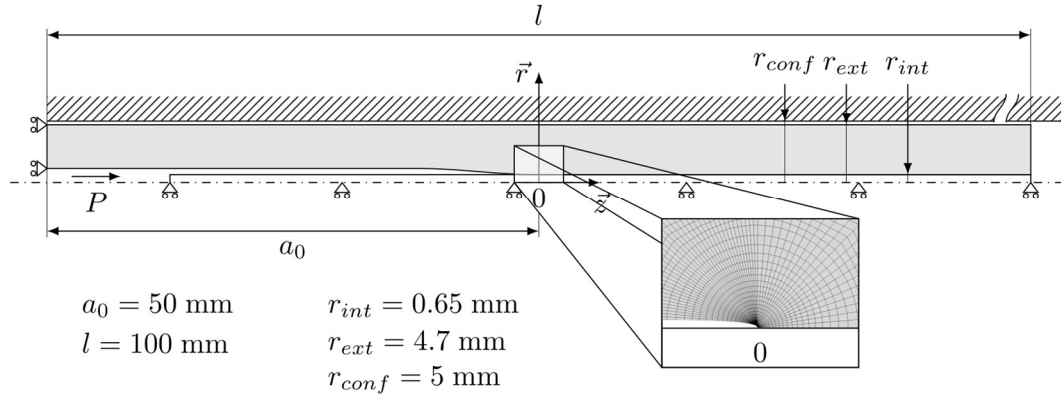
130 mechanisms. From the global energy balance analysis, the estimated G_C value incorporates all
131 these dissipation sources. According to the above presentation and previous contributions, a
132 reliable analysis of the RCAIT and G_C estimate requires proper monitoring of crack
133 propagation, fluid pressure, injected fluid volume and specimen deformation. Also, the
134 influence of additional dissipation mechanisms should be evaluated.

135 **3. Finite Element modelling of the RCAIT**

136 Up to now, the analysis of the experimental data from the RCAIT is essentially funded on
137 conclusions drawn from the TTRIM results [10] [16] and global energy balance evaluation.
138 This 1D model is applicable to the regime preceding the crack propagation step and describes
139 the inflation of an infinite pressurized rubber tube whether it is confined or not. However, the
140 influence of the specimen clamping region and the vicinity of crack tip position are not
141 considered. Finally, it would be relevant to assess the energy balance analysis during the crack
142 propagation regime by reproducing with a complete finite element simulation both crack
143 nucleation and propagation regime. Finally, the self-similar nature of the crack propagation
144 regime could be confirmed.

145 **3.1. Model description and preliminary hyperelastic analysis**

146 In the following, all finite element simulations use Abaqus© code. The model geometry
147 and boundary conditions of the model are presented in Figure 2 so as the mesh in the vicinity of
148 crack tip position. Due to specimen geometry and loading conditions, 2D axisymmetric
149 simulations are performed and cylindric coordinates system $(\vec{r}\vec{\theta}\vec{z})$ is considered. Due to the
150 mechanical contrast between the rubber and steel, the cord reinforcement is modelled as a rigid
151 line placed at a distance 0.65mm from the cylinder axis. The cord displacement is free along
152 direction \vec{z} but other degrees of freedom are set to zero ($U_r = R_\theta = 0$). The rubber envelop
153 outer radius is $r_{int} = 4.7\text{mm}$ and is represented with a rectangular solid surface.



154

155
156

Figure 2. Geometry, boundary conditions and mesh topology of the finite element model for crack onset study. The pre-crack opening is exaggerated for visualisation.

157

In the present analysis a detailed analysis of the clamping condition is not proposed.

158

Assuming the clamping region length is small compared to the pre-cracked distance, the

159

contribution of clamping region deformation on the overall injected volume will be assumed

160

negligible. Therefore, the clamped side of the specimen is simply replaced by the kinematic

161

condition ($U_z(z = 0) = 0$) corresponding to free radial expansion of the rubber tube across

162

section. Along the \vec{z} direction, the rubber envelop is partially bonded to the cord. The length

163

along which antiadhesive coating is deposited is considered as a pre-crack length, the presence

164

of film or coating is not explicitly considered in the simulation except by introducing

165

discontinuity between the two materials. Interphase region between rubber and cord is not

166

considered either and the bonding between the cord and the rubber is simply modelled with a

167

displacement continuity condition at the interface between rubber and cord.

168

A focus ring of element meshes the interface singularity region. 2D axisymmetric

169

quadrangle elements with quadratic interpolation are chosen. Full integration and hybrid

170

formulation scheme (*viz.* CAX8H in Abaqus) are used to manage material incompressibility.

171

All present computations use the implicit solver of Abaqus and the hypothesis of finite strain.

172

Finally, the 5mm inner radius confinement tube is introduced. Again, the mechanical

173

contrast between rubber and glass tube is very large so that the confinement tube can be

174 modelled as fixed rigid body. Considering that the lubrication between the glass tube and rubber
175 is efficient, the contact between the rubber envelop and the confinement is modelled as
176 frictionless contact using node to surface and penalty algorithm. Various loading conditions can
177 be applied to the inner radius of the rubber envelope (pressure, volume variation, ...) which are
178 detailed below.

179 The Exp-Ln strain energy potential [17] is used to derive the rubber material constitutive
180 law, as given in equation (2):

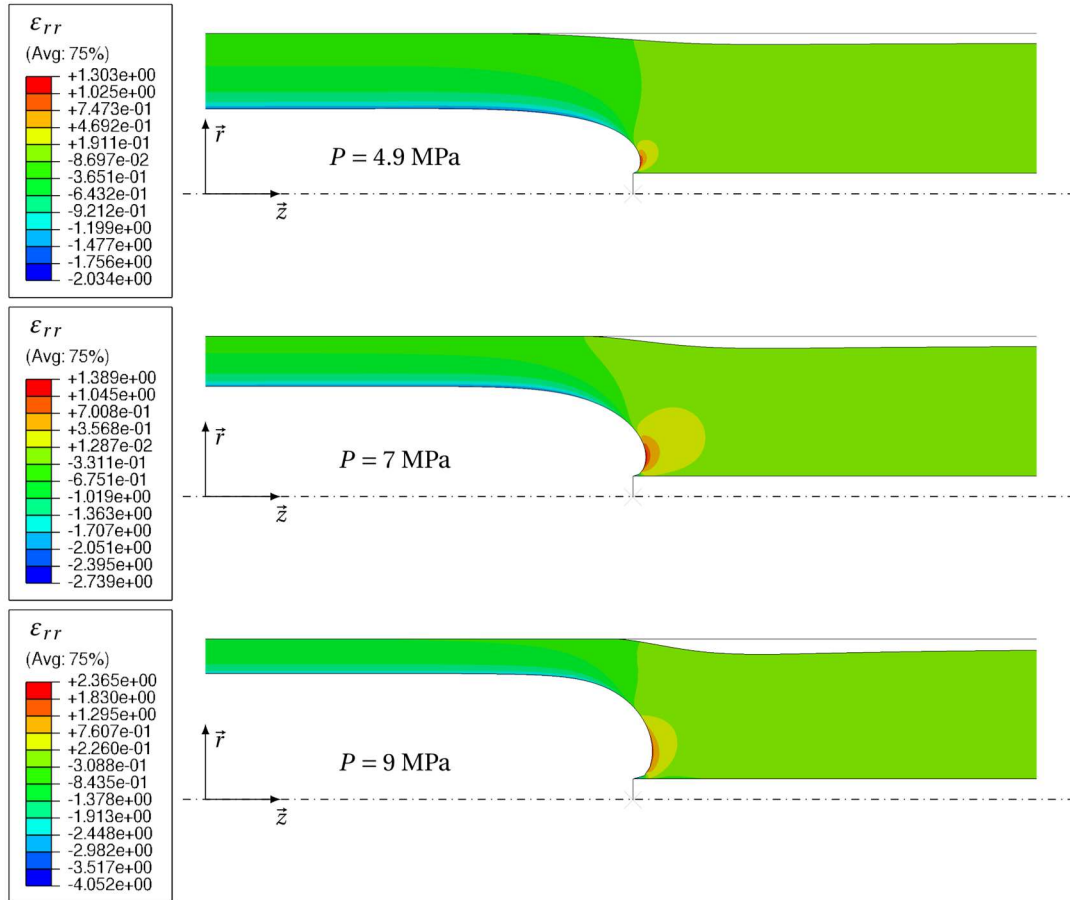
181

$$W = A \left[\frac{1}{a} \exp(a(I_1 - 3)) + b(I_1 - 2)(1 - \ln(I_1 - 2)) - \frac{1}{a} - b \right] \quad (2)$$

182

183 The expression of the strain energy density function only depends on the first invariant I_1 of the
184 transformation gradient. The Exp-Ln strain potential is applicable to natural rubbers reinforced
185 with black carbon which exhibit hardening for large elongation values. Material parameters A ,
186 a and b values used for the simulation have been identified previously ($A = 1.29$ MPa, $a =$
187 -1.19 , $b = -0.87$) [9]. The constitutive law is implemented in the finite element code
188 Abaqus© using the UHYPER subroutine.

189 In Figure 3 is represented the deformed configuration of the specimen for several
190 inflation pressure values up to 9 MPa as determined with the finite element model. The
191 maximum pressure value corresponds to the one measured experimentally when the decohesion
192 of the rubber / cord interface propagates. A 4.9 MPa pressure value is found for the end of the
193 free rubber expansion regime and start of rubber envelope to confinement tube contact ($r_{ext} =$
194 r_{conf}). Then, at higher pressure, the confinement tube tends to constrain the rubber envelop
195 radial expansion. Meanwhile, the axial expansion along the tube axis tends to increase rapidly
196 with the pressure.



198

199 **Figure 3** Opening logarithmic deformation ϵ_{rr} at different pressure for the crack onset model.

200

201 These results may seem similar to the one observed in other contributions [18], [19] where

202 elastomer / metal delamination mechanisms are discussed and modelled. However, peel like

203 mechanical test procedures are generally considered which leads to very different stress / strain

204 fields in the fracture process zone region compared to the RCAIT situation. The main difference

205 lies in the fact that due to the axisymmetric situation, the crack front is circular and

206 homogeneous plane strain condition is achieved all along the crack front. As also observed

207 when strong adhesion is achieved between rigid and soft bodies, a blunted crack tip is observed

208 at a finite distance from the rubber / metal interface. The initial stress singularity located at the

209 crack tip position vanishes since the rubber / cord contact angle becomes very small [20] [21].

210 Such result is consistent with previously observed fractured surface where a thin layer of

211 residual rubber was observed on the cord after complete failure. The mapping of the ε_{rr}
212 distribution in the specimen section does not illustrate the modification of the rubber loading
213 condition from mainly radial to longitudinal expansion but clearly enlighten the presence of
214 large circumferential stress concentration along the blunted crack tip at a finite distance from
215 the rubber / cord interface.

216 Now that the initial stage preceding the crack onset has been described, additional features
217 should be added to the finite element calculations to simulate the crack initiation and
218 propagation steps. Due to the presence of the initially sharp crack tip, numerical convergence
219 of the node-release crack propagation technique is difficult to achieve. More advanced methods
220 such as phase field, X-FEM are numerically costly and specific formulation and implementation
221 are required to describe the fluid injection process. The main objective of the present model
222 focused is to analyse the macroscopic response of the RCAIT specimen trying to capture the
223 overall response of the rubber envelope so as its interaction with the fluid and the confinement
224 tube. Nevertheless, numerous highly nonlinear phenomena can be evidences (large
225 displacements and rotations, hyperelastic behaviour, contact, ...). It seems difficult to capture
226 these macroscopic phenomena together with a fine description of the damage processes at the
227 crack tip position which could be studied in a second step. A phenomenological description is
228 then chosen to model the interface decohesion.

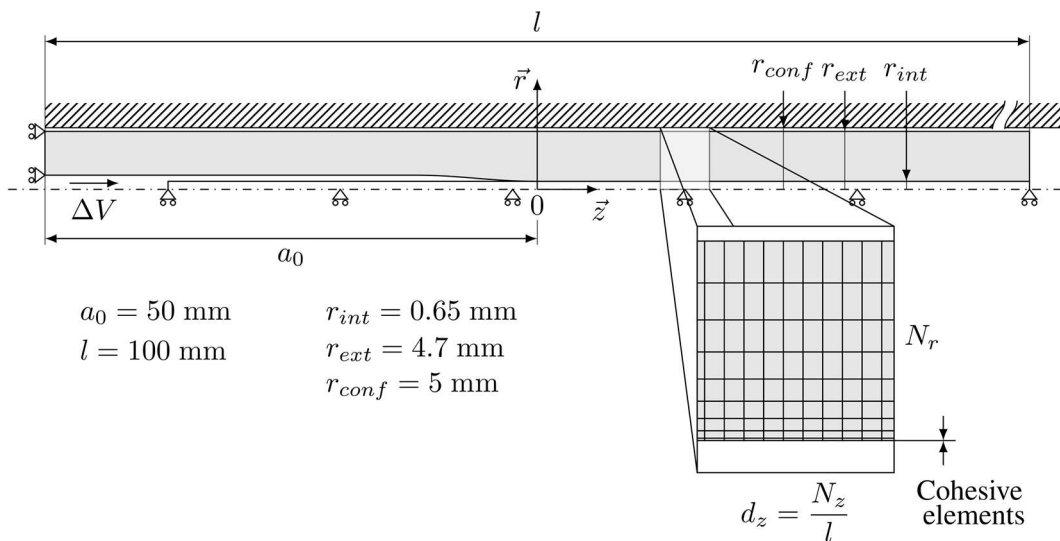
229 **3.2. Cohesive zone modelling of crack nucleation**

230 Since the crack path is known, a cohesive zone modelling (CZM) approach seems
231 appropriate as proposed in previous contributions [18] [22] [23]. Indeed, using CZM allows to
232 simulate both the decohesion nucleation and propagation regimes of the interfacial region
233 between the rubber and the cord. Phenomenological description is then achieved since the
234 cohesive elements are not capable to describe the complexity of the damage processes at the

235 crack tip. However, after appropriate calibration, a damage process zone with physical extend
 236 should be observed and a sensitivity to mode mixity loading conditions can be introduced.
 237 So, a layer of cohesive elements is introduced in between the rubber material and the solid line
 238 representing the rigid cord. Using Abaqus cohesive elements is preferred rather than cohesive
 239 surface interaction following recommendation from [24] for finite strain considerations.
 240 Abaqus surface interaction integrates the cohesive model on current configuration, while
 241 cohesive element maps back to the initial configuration. It leads to large difference over 10%
 242 in the effective work of fracture in the case of an elastomeric peel test from a rigid substrate.

243 The model including cohesive elements is quite similar to one presented in section 3.1.
 244 However, the introduction of cohesive elements needs to modify the mesh topology. Mesh and
 245 boundary conditions applied to the finite element model are presented in Figure 4. A grid-like
 246 mesh topology is used for the rubber envelope with higher element density nearby the inner
 247 radius were large elongation gradient are expected. Quadratic size distribution is used, therefore
 248 the mesh density along \vec{r} is given by the total number of elements in the radial direction N_r , set
 249 at 20 elements. 2D axisymmetric quadrangle elements with linear interpolation (CAX4H) are
 250 chosen to ensure connectivity with the rest of elements.

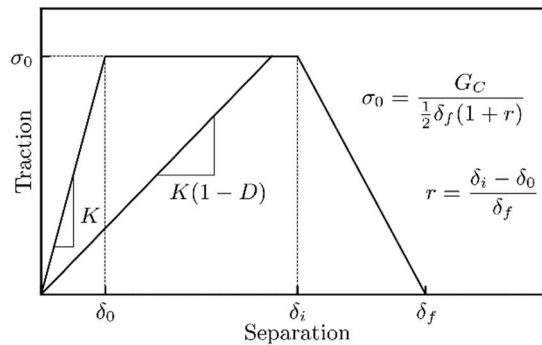
251



252

253 **Figure 4.** Geometry, boundary conditions and mesh topology of the finite element model including
 254 cohesive elements. The pre-crack opening is exaggerated for visualisation.

255 Cohesive elements are inserted between the rubber envelop and the rigid cord along half of
 256 the total length, with element density equal to $d_z = 4$, to bond the cord to the rubber envelop.
 257 Cohesive elements COHAX4 from the element library of Abaqus© with an initial zero
 258 thickness are used (see Figure 4). The cohesive element length is identical to the rubber mesh
 259 (0.25 mm). The cohesive element is formulated with a 2D axisymmetric hypothesis, linear
 260 interpolation and a Newton-Cotes integration scheme. As discussed above, the detailed
 261 description of the mechanical fields and damage processes close to the rubber / cord interface
 262 is replaced by a one-dimensional phenomenological description of the overall decohesion
 263 process. The cohesive model controls the evolution of cohesive stresses normal and tangent to
 264 the interface as a function of the relative displacement across the interface until complete
 265 decohesion. A phenomenological stress versus displacement evolution should be calibrated so
 266 that the simulated overall specimen response is found similar to the one observed
 267 experimentally. As main parameters, the cohesive element stiffness, K , should be chosen so
 268 that no significant softening is introduced during the elastic loading regime. Also, the CZM
 269 parameters (*viz.* max. relative displacement, δ_f , ultimate stress, σ_0 , ...) should be chosen so as
 270 to respect the energetic criteria controlling the complete decohesion of the interface.



271
 272 **Figure 5** Shape of the trapezoidal traction-separation law to model the interface.

273 In the present RCAIT configuration, the crack nucleation intermediate regime cannot be
274 distinguished for the reversible loading regime prior crack propagation occurs by analysing
275 $P(\Delta V)$ or $P(\lambda_z)$ evolutions. This suggest that the fracture process zone extend remains small
276 compared to other dimensions so that linear elastic fracture mechanics is applicable. CZM
277 parameters should be chosen also to observe limited extend of the fracture process zone on the
278 simulations. A triangular interface separation law is generally adopted for cohesive element
279 [18] [23] [22] over trapezoidal or exponential laws. However, large fracture process zone is
280 generally observed which are not consistent with the experimental observations. Then, a
281 trapezoidal law is preferred here with an additional shape parameter, r , which controls the
282 plastic regime extend, is used. A higher energy dissipation can be introduced while keeping a
283 same critical stress and critical relative displacement at break. Interface separation law is
284 represented in Figure 5. In the following, the nominal interface “stiffness”, K , and shape
285 parameter, r , will be kept constant. Indeed, K , is set so that the overall specimen stiffness
286 response is not altered with respect to the rigid interface situation. Meanwhile, the critical strain
287 energy release rate G_c is set arbitrary in a range of values corresponding to the ones measured
288 experimentally. The critical stress σ_0 is directly linked to G_c , K , r and δ_f . Then δ_f , σ_0 and r are
289 chosen so as to obtained physically realistic fracture process zone (FPZ) configuration. As
290 evidenced in section 3.1 and generally observed in interface decohesion situation mixed mode
291 loading conditions are expected. Mixed mode failure criteria could then be introduced.
292 However, due to the lack of experimental data describing the effect of mode mixity on the
293 decohesion process in this situation it would be artificial to introduce supplementary
294 parameters. Then identical interface separation laws are used for both traction and shear
295 contributions. The stress criterion at damage initiation is quadratic and the damage evolution
296 rule also considers the coupling between peel and shear stresses. Simulations results will be

297 introduced later, once the method for coupling CZM with the fluid injection process will be
298 discussed.

299 **3.2. Modelling of fluid driven crack nucleation and propagation**

300 **3.2.1. Implementation of hydrostatic fluid element**

301 The RCAIT such as most mechanical characterization tests including blister tests are
302 not load controlled but kinematic controlled. Indeed, since the injected fluid is incompressible
303 and the compliance of the hydraulic circuit is considered negligible the experiment is driven by
304 fluid volume injection rate. A constant pressure is applied to the inner surface of the specimen
305 but the contour of the inner surface including the near crack tip region depends on the fluid /
306 structure interaction. Since large deformation and nonlinear hyperelastic behaviour are
307 introduced the pressure versus injected volume evolution, $P(\Delta V)$, is not linear either. Then
308 applying pressure load to the inner radius of the specimen along the decohesion as boundary
309 condition is not really representative of the test conditions. Kinematic conditions should be
310 applied in the numerical simulation which are representative of the pressurized fluid injection
311 rate control conditions. This is notably critical to simulate the crack propagation regime when
312 the fluid pressure is constant where numerical instability may arise unless artificial numerical
313 “viscosity” would be introduced. To control the volume variation inside the rubber envelope
314 rather than applying a pressure to the inner radius, hydrostatic elements from Abaqus elements
315 library are used . Such elements describe the mechanical behaviour of closed cavity filled with
316 either compressible (pneumatic) or incompressible (hydraulic) fluid. They introduce a simple
317 fluid-structure interaction through the hypothesis of constant pressure across the fluid volume
318 and assuming the effect of liquid inertia is negligible. This formalism was previously used for
319 mechanical study of pressurized vessel [25], air spring suspension [26], air filled closed-cell
320 foam [27] or multiple pneumatic crash cushion [28].

321 Numerically, a layer of fluid cavity limits elements (here FAX2) is introduced around
322 the enclosed space between the rubber and the cord interface. The FAX2 elements mesh the
323 boundary of the fluid cavity, sharing nodes with the corresponding surface. Then, a node placed
324 in the meshed cavity acts as an integration point to compute the pressure. For axisymmetric
325 situation, this node must lie on the axis of revolution.

326 As boundary condition, a prescribed quantity of fluid can be added to a cavity. This
327 parameter corresponds to the one set experimentally. Providing, the displacement of the inner
328 radius of the rubber envelope could be prescribed by the expansion of the fluid cavity at a given
329 expansion rate, a uniform pressure will be applied to the inner radius of the rubber envelope.

330 **3.2.2. Coupling fluid cavity element and cohesive element**

331 The simulation of fluid driven crack propagation remains a complex issue especially due to
332 the difficulty in controlling the application of the pressure loading to the newly created surface.
333 The simulation of the RCAIT is even more complex due to the large deformation of the medium
334 coupled to the fact that the injected fluid pressure is expected to be constant during the crack
335 propagation regime. Therefore, to achieve numerical stability, kinematic controlled loading
336 conditions should be applied. Therefore, the proposed strategy consists in introducing multiple
337 connected hydrostatic fluid cavity along the rubber / cord interface which will be filled with
338 fluid sequentially during the crack propagation regime to force the crack opening while the
339 decohesion extends. This solution is proposed since the pore pressure cohesive elements and
340 hydrostatic fluid cavities cannot be used together in a model in Abaqus. The main advantage of
341 the coupling presented here is the meaningful dialogue between the inflation of the pre-crack
342 length of the specimen and the newly cracked surface length. The coupling of the fluid cavity
343 is also possible with continuum element degradation or node-release crack propagation.

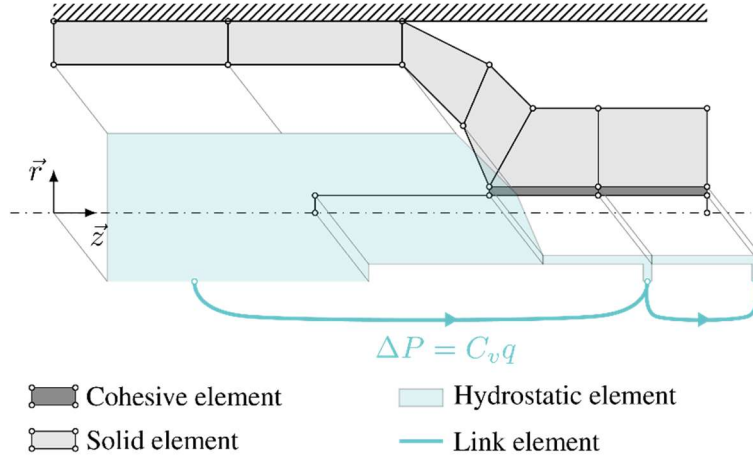


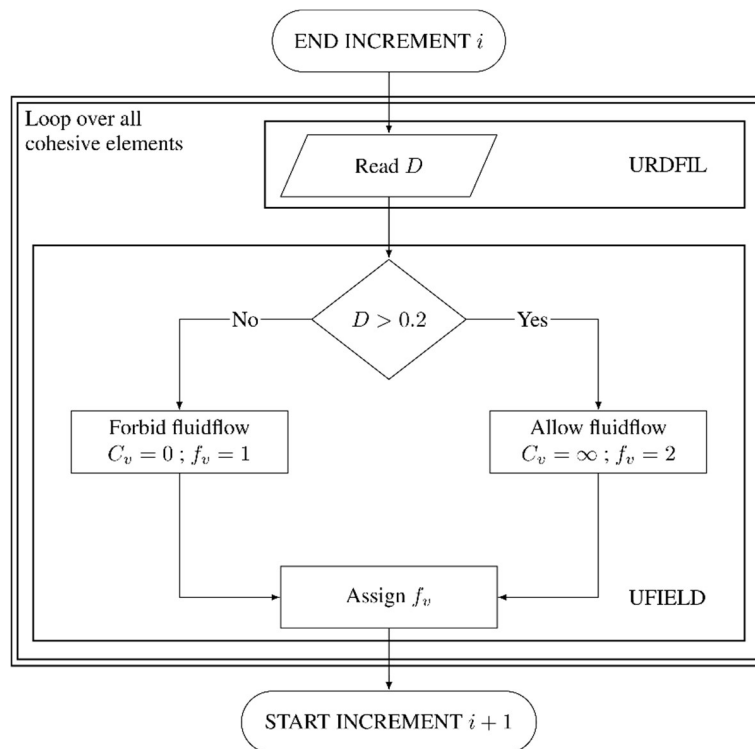
Figure 6 Illustration of the superposition of hydrostatic fluid element and cohesive elements (thickness of the cohesive elements is exaggerated) and connection between cavities.

344 The superimposition of initial mesh with the fluid cavity elements network describing the
 345 interaction between cohesive and fluid cavity elements is presented in Figure 6. A main fluid
 346 cavity maps the initial pre-crack length of the specimen. Then, a succession of fluid cavity is
 347 superimposed to each cohesive element. However, each cavity is extended up to the axis of
 348 revolution in order to compute the injected volume properly and allow to place the integration
 349 point of the cavity. These cavities are filled sequentially along the crack propagation path, fluid
 350 link elements are used to connect each successive cavity. The fluid flow from a first cavity to
 351 the following is given by the relation:

$$\Delta P = P_m - P_s = C_v q \quad (1)$$

352 Where ΔP is the pressure difference between first (pressure P_m) and following (pressure P_s)
 353 cavities, C_v is a viscous resistance coefficient and q is the fluid flow between the two cavities.
 354 This additional numerical parameter, C_v , should be calibrated so that no artificial rate
 355 dependence effect is observed. Also, the fluid link elements have a modifiable fluid behaviour
 356 since C_v can depend on ΔP , temperature or user defined field variables f_v . This last dependency
 357 is the key to the coupling between fluid cavities flow connection and cohesive elements
 358 degradation. Indeed, from physical standpoint, the flow of the fluid penetrating in the fracture

359 process zone may be dependent on local damage of the rubber. Then, the C_v coefficient value
 360 is updated during the simulation as a function of the damage level of the local cohesive element.
 361 For now, a simple cavity onset criterion is introduced considering the local fluid cavity element
 362 starts to fill once the damage variable D of the local cohesive element is more than 0.2. Indeed,
 363 it was observed that the numerical convergence is enhanced when the pressure is applied before
 364 the total degradation of the cohesive element is reached. Therefore, the pressure locally
 365 increases with the fluid flowing to the cavity and then introducing an intermediate process zone
 366 region where the internal pressure accelerates the damage process but also allows smooth
 367 injection of the fluid in the newly created area.



368

369 **Figure 7.** Flowchart of numerical procedure to combine fluid cavity and cohesive element and the
 370 breakdown between the two Abaqus subroutine.

371 The relation between fluid cavity element and damage is not a standard implementation
 372 in Abaqus. The algorithm depicted in Figure 7 is executed between each iteration of the finite
 373 element solver. First, the local damage value of each cohesive element is read with a URDFIL
 374 subroutine. Then, the subroutine UFIELD assigns a field variable, f_v , to each fluid link element

375 depending to the damage of cohesive element located at the slave cavity element. Two values
376 can be assigned to C_v . In case $D < 0.2$ then C_v is set to zero so that the fluid is blocked, in case
377 $D \geq 0,2$ then an incommensurable value is assigned to C_v so that the fluid fills the cavity
378 immediately at the next iteration. A Fortran COMMON BLOCK is used to retrieve damage
379 value from URDFIL subroutine and transmit them to the UFIELD subroutine.

380 With this numerical procedure the whole crack nucleation and propagation steps are simulated
381 reproducing the complete RCAIT. In particular, fluid driven crack propagation under constant
382 volume injection rate is achieved with stable crack propagation regime with constant fluid
383 pressure. Add to the cohesive zone parameters two additional parameters (onset, C_v) which
384 controls the pressurized fluid flow through the process zone.

385 **4. Cohesive zone modelling of the RCAIT**

386 In the following, the numerical procedure described above is used to reproduce theoretically
387 the experimental results obtained on a specimen made with NBR bonded to a brass coated steel
388 cord. After satisfactory agreement is found at a macroscopic scale, then the results from the
389 simulation are analysed to evaluate locally the conditions leading to crack nucleation and
390 propagation but also to discuss the limits of the proposed approach.

391 **4.1. RCAIT macroscopic response - experimental vs theoretical**

392 As discussed above, most of the material parameters controlling the response of the RCAIT can
393 be determine experimentally. Indeed, a simple hyperelastic model of the rubber behaviour has
394 been identified from uniaxial tensile tests data and evaluation of the RCAIT data along the
395 precrack length. The critical SERR of the rubber / cord interface is obtained from energy
396 balance analysis of the RCAIT, and rubber strength is obtained from tensile test results again.
397 The remaining parameters are mostly numerical ones except the remaining cohesive zone model
398 parameters (viz. r and δ_f). In the following, the shape factor is set arbitrarily to 85%. Indeed,

399 as for most cohesive zone models use cases, a high enough element density should be used to
 400 ensure appropriate description of the interface separation law along the FPZ. Then, $r = 0.85$
 401 was found satisfactory to obtain satisfying compromise between mesh density, numerical cost
 402 and description of the FPZ. Then a smooth development of damage along the process zone was
 403 found which is also a necessary condition to observe a progressive filling of the fluid cavity
 404 elements according to the scheme depicted in Figure 7. Then, the last parameter to be determine
 405 is the displacement jump leading to complete interface separation, δ_f , which is found equal to
 406 2.8mm. CZM parameters are finally summarized in Table 1.

407

G_C	K	σ_0	r	δ_f
80 KJ/m ²	1000 MPa	30 MPa	0.85	2.8 mm

408 **Table 1.** Cohesive zone model parameters.

409

410 In Figure 8 and Figure 9 are reported the main experimental data recorded during a RCAIT
 411 which are compared with the complete results of the RCAIT simulation describing decohesion
 412 nucleation and propagation regimes. It should be noted that the simulation is stopped before
 413 total delamination of the whole interface is observed considering the computation time. Indeed,
 414 for $G_C = 80 \text{ kJ/m}^2$, the simulation of a 1 mm crack propagation requires approximately 3 days
 415 of processing using 16 cpus at 2.60 GHz. In Figure 8, the injected fluid pressure, P , versus
 416 injected fluid volume shows satisfactory agreement for both the crack nucleation and
 417 propagation regime. Indeed, during the crack propagation regime, a same plateau pressure value
 418 is found which confirms the crack propagation behavior is controlled at the macroscopic scale
 419 by the only energy balance criteria. During the crack nucleation regime, very similar behaviour
 420 is observed. The experimental evolution exhibits more compliant behaviour so as abnormal
 421 preliminary inflation regime. Indeed, the specimen attachment condition are not precisely

422 modelled in the finite simulation nor the possible presence of air entrapped in the hydraulic
 423 circuit so that very stiff initial response is found numerical compared to the experimental result.
 424 Also, overall more compliant specimen behaviour is found experimentally due both to poor
 425 evaluation of the initial decohesion length value but also probably to underestimation of the
 426 inner radius of the rubber envelope since the presence of anti-adhesive film is not considered.

427

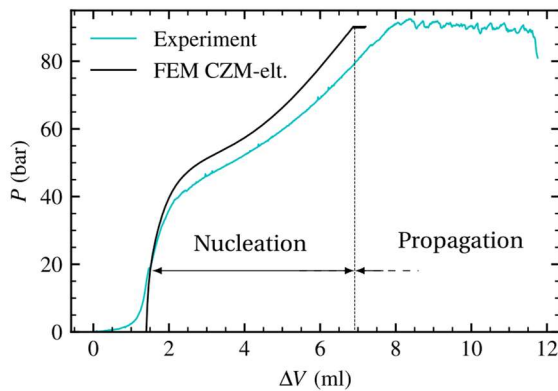


Figure 8 Comparison of experimental and numerical inflation curves

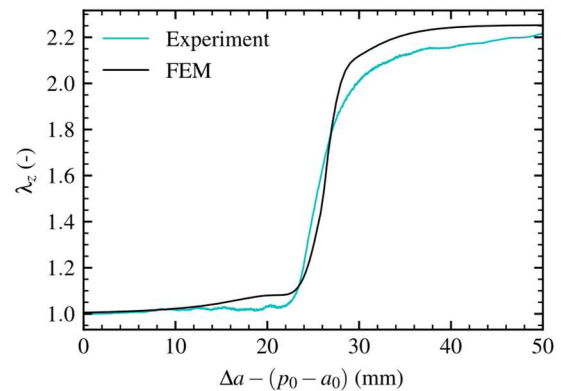


Figure 9 Comparison of experimental and numerical λ_z process zone

428

429 During the RCAIT, a marker tracking technique is implemented to evaluate the evolution of the
 430 longitudinal elongation at the outer radius position along the specimen axis. Experimental and
 431 theoretical evolutions are compared in Figure 9 and exhibit similar evolutions again. A small
 432 discrepancy is found on the plateau, λ_z , value in the inflated region of the specimen which may
 433 attributed to biased evaluation of the inner radius again, or experimental artefacts such as
 434 confinement tube / rubber residual friction. However, the two evolutions evidence identical
 435 shape and extend (*ca.* 20mm) of the transition region between bonded and fractured part of the
 436 specimen. For both Figure 8 and Figure 9 no significant feature allows to evidence the
 437 development of a FPZ at the interface scale which justifies the use of simple linear fracture
 438 mechanics approach to analyze RCAIT.

439

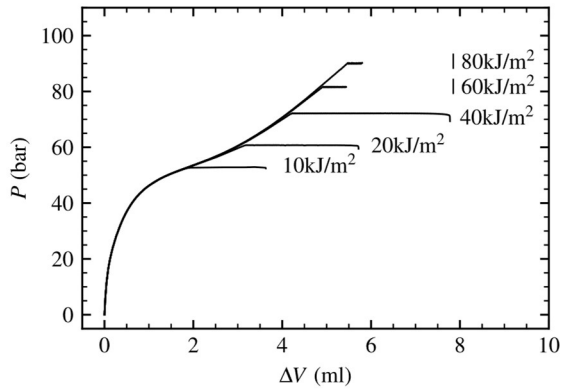


Figure 10 Inflation curves prediction of the cohesive modelling for different G_C value ($r=0.85$, $\delta_f = 2.9$ mm).

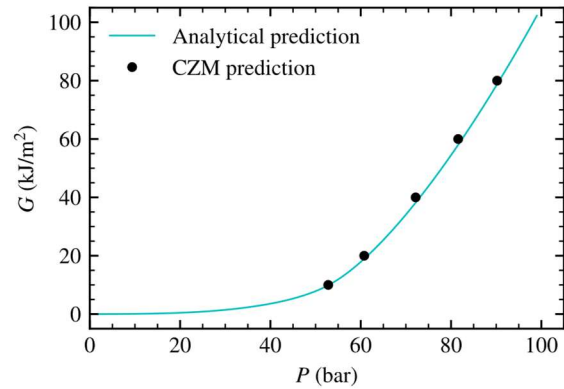
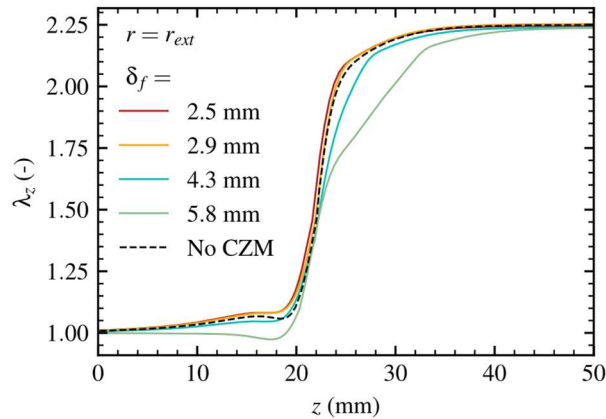


Figure 11 Comparison of analytical [10] and cohesive modelling prediction of critical pressure to propagation in function of critical SERR.

440 Then, using the same procedure, RCAIT are simulated again but considering different critical
 441 SERR values for the cohesive elements in the interval [10:80] kJ/m². All CZM parameters are
 442 kept the same except ultimate stress which is changed so as to obtain appropriate G_C value.
 443 Resulting fluid pressure versus injected volume evolutions are reported in Figure 10. All
 444 evolutions are found the same except the plateau pressure value which varies with the G_C value.
 445 The semi-analytical relation derived in [16] to evaluate G_C from the measure critical pressure
 446 value is compared with numerical results in Figure 11. Both analytical and numerical model
 447 predictions agree which demonstrates again that LEFM is valid to evaluate G_C . This indicates
 448 that the FPZ extend should be negligible compared to other characteristic dimension (rubber
 449 envelope thickness, initial decohesion, accommodation length ...) but also that the steady state
 450 crack propagation regime is observed after a small crack propagation distance.

451 It should be noted that the value of G_C as high as 80kJ/m² enforce a correct phenomenological
 452 description of the experiment. The dissipation during propagation comes both from the bulk
 453 material and the interface. Meanwhile, the model places all the dissipation in the cohesive
 454 element. And, as the crack surface is cylindrical, the G_C value is actually dependent of the
 455 radial position of the cohesive element.

4.2. Local analysis – Development of FPZ



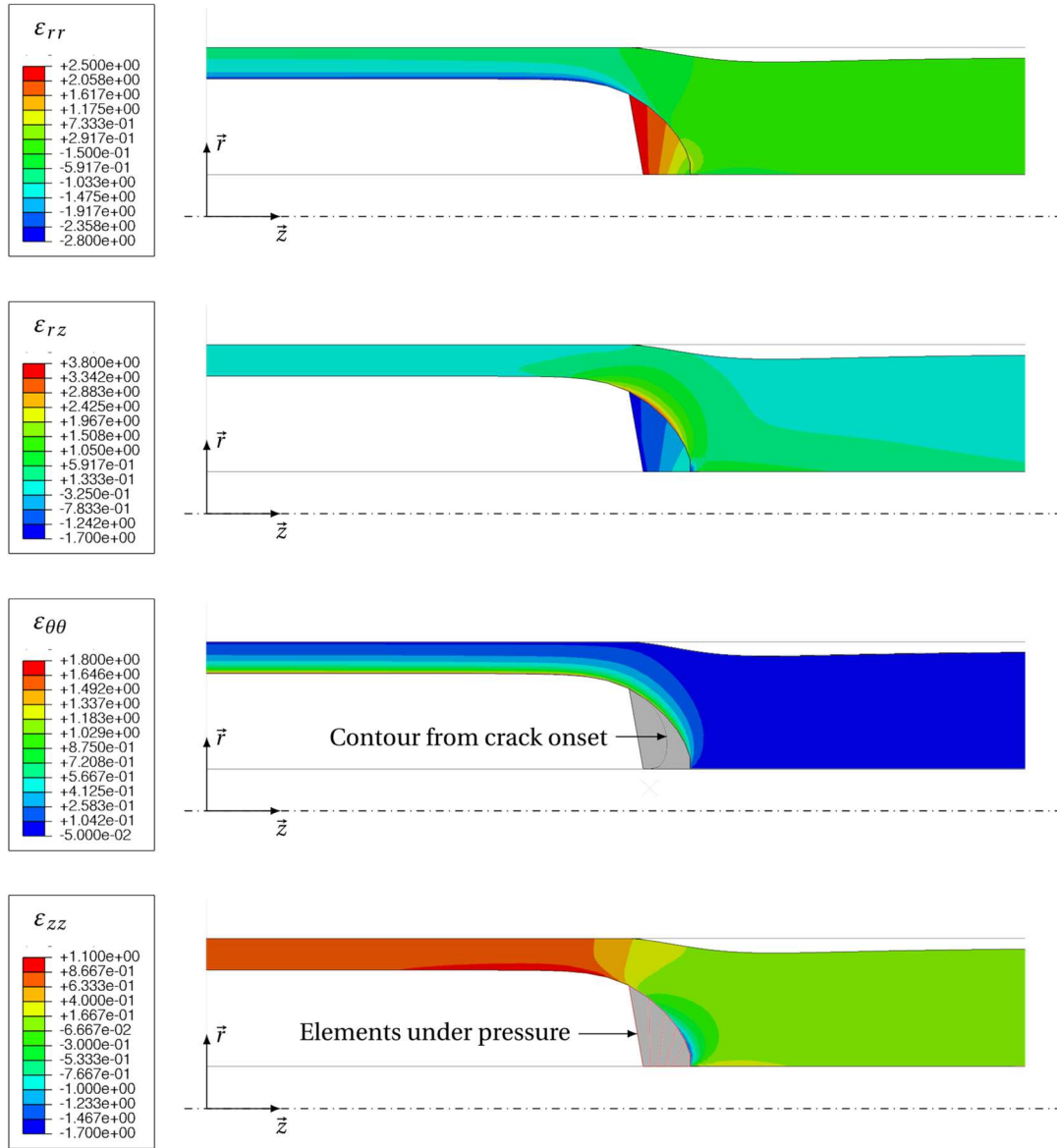
457
458
459
460

Figure 12 Comparison of the transition zone length on the exterior radius of the specimen for different displacement at complete failure for the cohesive zone model ($G = 80 \text{ kJ/m}^2$, $r = 0.85$)

461 The previous results seem to indicate that the macroscopic response of the RCAIT is little
462 affected by the exact shape of the interface separation law since non-features related to the
463 FPZ development was observed compared to a purely elastic analysis. However, to assess
464 this hypothesis a parametric analysis is performed by varying parameter, δ_f , and modifying
465 σ_0 accordingly so as to keep constant $G_C = 80 \text{ kJ/m}^2$ value. The resulting $\lambda_z(z)$ evolution
466 for all test cases are reported in Figure 12. For the two smaller values considered in this
467 study including the one used in section 4.1, the resulting evolutions are identical to the one
468 obtained for perfectly bonded interface. For a significant difference to be observed very
469 large δ_f values should be used leading to unrealistic FPZ extension. The total displacement
470 to failure can reach a size similar to the confinement radius r_{conf} while still reaching in a
471 steady-state propagation. Indeed, the confinement radius limits the opening displacement.
472 Nonetheless, if the element does not fail under opening mode for a small process zone, it
473 will undergo a shear loading. Therefore, while the opening displacement is limited by the
474 confinement radius, the shear displacement is limited only by the maximum axial elongation
475 of the fully cracked part of the specimen. Then the parameters given in Table 1 offers the

476 best compromises with the present mesh topology to reproduce the results obtained at a
 477 macroscopic scale.

478



479
 480 **Figure 13** Cartography of the strain tensors value around the crack tip during propagation.

481

482 In Figure 13 are reported the cartography of the radial elongation in the specimen cross section,
 483 and contour also presented in section 3.1 to evidence the presence of strong stress concentration
 484 at the blunted crack tip position. The contour of the reference configuration (rigid interface) for
 485 the same injected fluid pressure value is superimposed with the result of the cohesive zone

486 modelling. Both contour match except in the vicinity of the crack tip position where the
487 presence of a cohesive element strongly modifies the contact angle between rubber and cord
488 and more generally the near cord region. These pictures illustrate the phenomenological nature
489 of the proposed modelling strategy which requires careful calibration of the CZM parameters
490 as a function of the mesh topology and consequently its limitations. Indeed, the CZM modelling
491 aims to describe the rubber / cord interface decohesion. From Figure 3, it is clear that the crack
492 will initiate and propagate from the stress concentration region located at a finite distance from
493 the interface. The CZM parameters are then representative of the decohesion of the near cord
494 region over a finite distance rather than the one of the interface unless very small element size
495 are used. Indeed, with the present mesh topology no crack propagation is observed with the
496 CZM when too small δ_f values are used (and consequently large σ_0) since due to the element
497 distortion at the crack tip position, the normal stress in the cohesive element becomes
498 compressive and blocks the development of any damage. δ_f values are finally representative of
499 the radial position of the blunted crack tip when crack propagation starts.

500 At last, the damage value in the cohesive elements are reported which are also representative
501 of the pressure of the local fluid cavity element and applied to the inner contour of the rubber
502 interface. As seen in Figure 13, by filling the fluid cavity when the damage value in the cohesive
503 element is larger than 0.2, the fluid pressure is applied to most of the inner contour of the rubber
504 envelope so that the resulting deformation is similar to the one obtained by considering a rigid
505 interface. As a conclusion, the present finite element procedure is capable to describe both crack
506 nucleation and propagation sequence during RCAIT and the overall macroscopic response
507 including the regular stress and elongation fields in the rubber envelope. However, CZM
508 remains phenomenological so that calibration is required. Such macroscopic description then
509 fails in describing the exact nature of the process zone, however the identified CZM parameters
510 are representative of specimen configuration.

511

512 4.3. Loading paths during crack propagation

513 In previous contributions, the analysis RCAIT uses the only one-dimensional TTRIM which
 514 doesn't consider the three-dimensional nature of the stress and elongation fields in the
 515 accommodation region. Also, the TTRIM only describes the initial inflation regime of the
 516 precrack region but not the crack propagation regime. Capturing the exact loading path in the
 517 specimen could be important to better evaluate the dissipative mechanisms in the rubber during
 518 crack propagation.

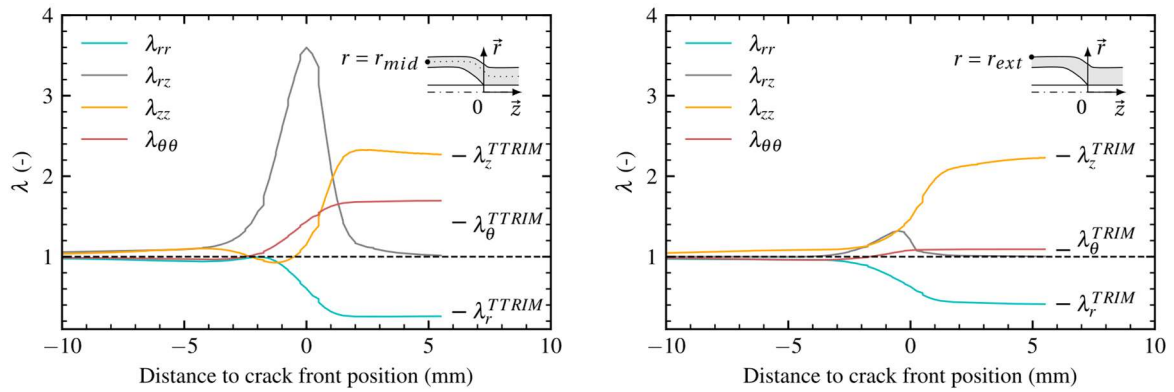
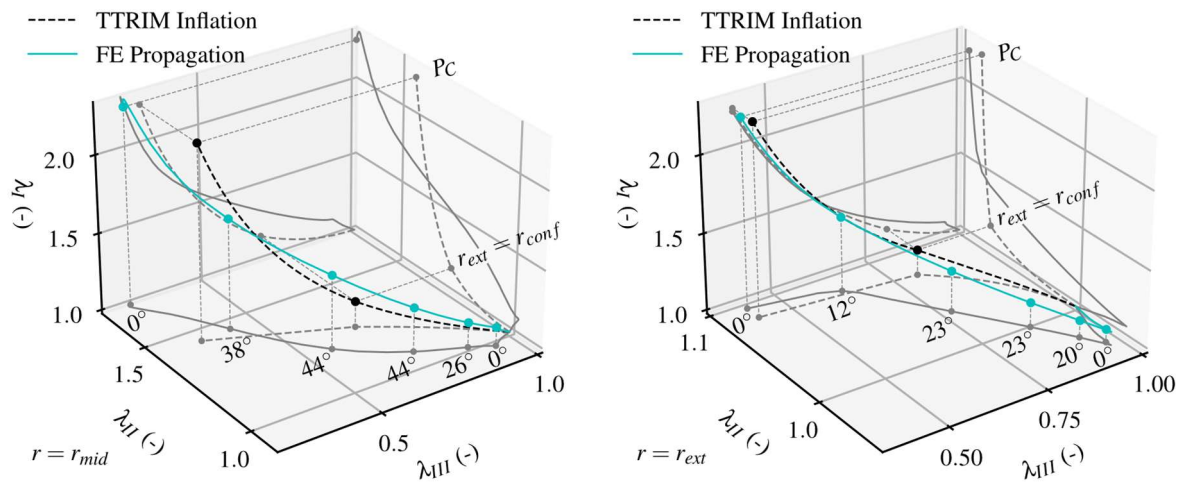


Figure 14 Evolution of the elongation of an element of matter in the middle and the exterior of the rubber envelop as the cord delamination advances ($\sigma_0 = 30 \text{ MPa}$, $r = 0.85$, $G_C = 80 \text{ kJ/m}^2$)

519

520 To illustrate this, the evolution of the local elongations of a given element during crack
 521 propagation is reported. The evolutions are plotted as a function of the instant distance to crack
 522 tip position so that in an Eulerian representation of a steady state crack propagation regime,
 523 these evolutions are similar to their spatial evolutions along the specimen for a given crack tip
 524 position. Two radii are considered, on the outer skin and the mid through thickness position. As
 525 the finite element can only capture globally the strain field around crack tip, a loading path on
 526 the inner radius is omitted. Also, the value determined with the TTRIM are reported. These
 527 evolutions are found the same whatever the element is chosen at the same radial position along
 528 the crack propagation direction which confirms the self-similar nature of the crack propagation

529 regime. Also, these simulations clearly reveal the multiaxial nature of the rubber loading
 530 condition during crack propagation also predicted with the TTRIM.



531 **Figure 15** Comparison of loading path in principal stretches space between inflation (TTRIM
 532 analytical) and propagation (FE CZM) at two radii. Rotation angle between the FE and the analytical
 533 eigenspaces is reported on FE loading path.

534

535 However, a significant shear deformation is found along the accommodation length which is
 536 not predicted with the TTRIM. In Figure 15, the two loading paths are compared in the principal
 537 stretches space, at the middle and the exterior of the rubber envelop. The two paths are similar
 538 at the exterior radius, while a difference appear at the mid radius. Moreover, the shear
 539 component is predominant on a large amount of the path. The analytical solution has an
 540 eigenspace corresponding to the global coordinates $(\vec{r}\vec{\theta}\vec{z})$, while the FE CZM eigenspace has
 541 an angle with respect to the global coordinates. An angle value of 0° indicates only
 542 traction/compression deformation and 45° , only shear deformation. The angle is higher on the
 543 mid radius than on the exterior radius, meaning higher shear state closer to the interface. Thus,
 544 the local rubber and interface loading condition is different from the early analysis with the
 545 TTRIM and indicates that shear behaviour characterization of the rubber would be needed for
 546 proper hyperelastic model calibration.

547 **5. Conclusion**

548 In the present contribution, a simulation of the complete RCAIT considering fluid driven crack
549 propagation test under constant injection rate condition is achieved. Original implementation is
550 proposed here consisting in coupling fluid cavity elements with cohesive zone elements. The
551 load application conditions over the whole crack nucleation and propagation process are
552 reproduced from which the self-similar nature of the crack propagation can be observed associated
553 to a fluid injection pressure value. The model calibration uses mainly data directly obtained
554 from macroscopic tests (rubber behaviour, rubber strength, specimen fracture energy). Indeed,
555 with the actual specimen geometry, the experimental data recorded during the test can be
556 reproduced with simple LEFM consideration and hyperelastic modelling of the rubber inflation.
557 Then little / no influence of the CZM parameter is found except G_C . Other two parameters K ,
558 r , δ_f are chosen essentially to ensure numerical convergence and realistic FPZ extension. to
559 propagation dictated by the critical strain energy release rate. With this model a more complete
560 picture of the RCAIT condition is obtained and the self-similar nature of the crack propagation
561 condition is validated. While the detailed description of the FPZ is not achieved, a more realistic
562 description of the accommodation region is obtained which exhibits large shear deformation
563 values which are not predicted with the TTRIM where maximum deformation state could be
564 reached.

565 Multiple perspectives regarding the application of the present RCAIT finite element model can
566 be drawn. First the model can be used for a better estimate of the influence of test boundary
567 conditions. In particular, the effectiveness of rubber to confinement tube lubrication could be
568 assessed by introducing friction contact. Additional bulk dissipative mechanisms apart from the
569 one developing in the FPZ can now be introduced in the rubber behaviour such as softening [29]
570 and viscosity with the objective to deconvolute these contributions from the one driving locally
571 the crack propagation. Finally, these results could be assessed with supplementary experimental

572 observations which may require the use of tomographic equipment to image the specimen
573 section during crack propagation.

574 **6. Acknowledgement**

575 Authors would like to thank the Region Bretagne for its financial support through ARED grant.

576 **Bibliographie**

577

- [1] A. Lechtenboehmer, H. G. Moneypenny et F. Mersch, «A Review of Polymer Interfaces in Tyre Technology,» *Brit. Poly. J.*, vol. 22, n° 4, pp. 265-301, 1990.
- [2] W. J. Van Ooij, «Surface composition, oxidation and sulfidation of cold-worked brass and brass-coated steel wire as studied by x-ray photoelectron spectroscopy I. Surface composition of commercial cold-worked brass,» *Surface Technology*, vol. 6, n° 1, pp. 1-18, 1977.
- [3] P. Sarkar et A. K. Bhowmick, «Sustainable rubbers and rubber additives,» *J. Appl. Polym. Sci.*, vol. 135, n° 24, p. 45701, 2018.
- [4] D. Nicholson, D. Livingston et G. Fielding-Russell, «A New Tire Cord Adhesion Test,» *Tire Science and Technology*, vol. 6, n° 2, pp. 114-124, 1978.
- [5] M. D. Ellul et R. J. Emerson, «A new pull-out test for tire cord adhesion - Part I. Hot Bonding,» *Rubber Division Meeting, American Chemical Society*, 1987.
- [6] R. Brown, «Adhesion, corrosion and staining,» *Physical Testing of Rubber*, p. 299–316, 1996.
- [7] A. N. Gent et O. H. Yeoh, «Failure loads for model adhesive joints subjected to tension, compression or torsion,» *J. Mater. Sci.*, n° 17, pp. 1713-1722, 1982.
- [8] G. J. Lake, «Fracture Mechanics and its Application to Failure in Rubber Articles,» *Rubber Chemistry and Technology*, vol. 76, n° 3, p. 567–591, 2003.
- [9] P.-Y. Corbel, J. Jumel, K. Kane et A. Mbiakop-Ngassa, «Refined crack propagation methodology and energy balance analysis in the Rubber Cord Adhesion Inflation Test,» *International Journal of Adhesion and Adhesives*, vol. 119, p. 103243, 2022.

- [10] K. Kane, J. Jumel, F. Lallet, A. Mbiakop-Ngassa, J. M. Vacherand et M. E. R. Shanahan, «A novel inflation adhesion test for elastomeric matrix/steel cord,» *International Journal of Solids and Structures*, vol. 160, pp. 40-50, 2019.
- [11] H. Dannenberg, «Measurement of Adhesion by a Blister Method,» *Journal of Applied Polymer Science*, vol. 5, n° 14, pp. 125-134, 1961.
- [12] Y. S. Chang, Y. H. Lai et D. A. Dillard, «The constrained blister - a nearly constant strain energy release rate test for adhesives,» *J. Adhes.*, vol. 4, n° 27, pp. 197-211, 1989.
- [13] B. Paul, M. Faivre, P. Massin, R. Giot, D. Colombo, F. Golfier et A. Martin, «3D coupled HM–XFEM modeling with cohesive zone model and applications to non planar hydraulic fracture propagation and multiple hydraulic fractures interference,» *Computer Methods in Applied Mechanics and Engineering*, n° 342, pp. 321-353, 2018.
- [14] W. A. C. Jin, «Fluid-driven transition from damage to fracture in anisotropic porous media: a multi-scale XFEM approach,» *Acta Geotechnica*, n° 15, pp. 113-144, 2020.
- [15] C. Chukwudozie, B. Bourdin et K. Yoshioka, «A variational phase-field model for hydraulic fracturing in porous media.,» *Computer Methods in Applied Mechanics and Engineering*, vol. 347, pp. 957-982, 2019.
- [16] K. Kane, J. Jumel, A. Mbiakop-Ngassa, F. Lallet, J. M. Vacherand et M. E. R. Shanahan, «Rubber cord adhesion inflation test: Effect of the constitutive rubber model on evaluation of G_c ,» *Engineering Fracture Mechanics*, vol. 244, p. 107547, 2021.
- [17] H. Khajehsaeid, J. Arghavani et R. Naghdabadi, «A hyperelastic constitutive model for rubber-like materials,» *European Journal of Mechanics - A/Solids*, vol. 38, pp. 144-151, 2013.
- [18] K. M. Liechti et J.-D. Wu, «Mixed-mode, time-dependent rubber/metal debonding,» *Journal of the Mechanics and Physics of Solids*, vol. 49, n° 5, pp. 1039-1072, 2001.
- [19] J. Neggers, J. P. Hoefnagels, O. van Der Sluis, O. Sedaghat et M. G. Geers, «Analysis of the dissipative mechanisms in metal–elastomer interfaces,» *Engineering Fracture Mechanics*, vol. 149, pp. 412-424, 2015.
- [20] V. R. Krishnan et C. Y. Hui, «Finite strain stress fields near the tip of an interface crack between a soft incompressible elastic material and a rigid substrate,» *Eur. Phys. J. E*, vol. 29, pp. 61-72, 2009.
- [21] T. H. Lengyel, R. Long et P. Schiavone, «Effect of interfacial slippage on the near-tip fields of an interface crack between a soft elastomer and a rigid substrate,» *Proceedings of the Royal Society A: Mathematical, Physical and Engineering Sciences*, vol. 470, n° 2170, pp. 1364-5021, 1471-2946, 2014.

- [22] B. Mukherjee, D. A. Dillard, R. B. Moore et R. C. Batra, «Debonding of confined elastomeric layer using cohesive zone model,» *International Journal of Adhesion and Adhesives*, vol. 66, pp. 114-127, 2016.
- [23] Q. Meng et M. Chang, «Interfacial crack propagation between a rigid fiber and a hyperelastic elastomer: Experiments and modeling,» *International Journal of Solids and Structures*, vol. 188, pp. 141-154, 2020.
- [24] P. Gilormini et J. Diani, «Testing some implementations of a cohesive-zone model at finite strain,» *Engineering Fracture Mechanics*, n° 148, pp. 97-109, 2015.
- [25] T. Rumpel et K. Schweizerhof, «Hydrostatic fluid loading in non-linear finite element analysis,» *Int. J. Numer. Meth. Engng.*, vol. 59, n° 6, pp. 849-870, 2004.
- [26] D. T. Berry et H. T. Y. Yang, «Formulation and experimental verification of a pneumatic finite element,» *Int. J. Numer. Meth. Engng.*, vol. 39, n° 7, pp. 1097-1114, 1996.
- [27] N. J. Mills, R. Stämpfli, F. Marone et P. A. Brühwiler, «Finite element micromechanics model of impact compression of closed-cell polymer foams,» *International Journal of Solids and Structures*, vol. 46, n° 3-4, pp. 677-697, 2009.
- [28] C. Graczykowski et J. Heinonen , «Feasibility study of adaptive inflatable structures for protecting wind turbines,» *Journal of Structural Mechanics*, vol. 40, n° 2, pp. 7-23, 2007.
- [29] L. Mullins, «Softening of Rubber by Deformation,» *Rubber Chemistry and Technology*, vol. 42, n° 1, pp. 339-362, 1969.

578

579